Electrochimica Acta 416 (2022) 140288

Contents lists available at ScienceDirect

Electrochimica Acta

journal homepage: www.journals.elsevier.com/electrochimica-acta

Locally sculptured modification of the electrochemical response of conductive poly(lactic acid) 3D prints by femtosecond laser processing

Mateusz Cieslik [a], Miroslaw Sawczak [b], Rafal Jendrzejewski [b], Joanna Celej [c], Wojciech Nogala [c], Jacek Ryl [a,*]

[a] Gdansk University of Technology, Narutowicza 11/12, Gdansk 80-233, Poland
[b] The Szewalski Institute of Fluid-Flow Machinery, Polish Academy of Sciences, Fiszera 14, Gdansk 80-231, Poland
[c] Institute of Physical Chemistry, Polish Academy of Sciences, Kasprzaka 44/52, Warsaw 01-224, Poland

ARTICLE INFO

Keywords:
Polymer-matrix composite
Electrochemical behaviour
3D printing
Femtosecond laser ablation

ABSTRACT

This manuscript presents an approach to sculpture high electrochemical activity of the 3D printed electrodes with poly(lactic acid) (PLA) matrix and carbon black (CB) filler by femtosecond laser (FSL) ablation. CB-PLA utility for electrochemical applications depends on a surface modification aiming to remove the PLA and uncover the conductive CB. We have discussed how laser pulse energy is critical for such an activation process. The best performance was obtained for 4.1 J cm^{-2}, while scanning electron microscopy (SEM) shows only partial evaporation of PLA at lower energy densities. Next, we have confirmed the efficiency of locally sculptured CB-PLA surface activation by FSL treatment, obtaining high linearity between electrochemically active surface and FSL-treated surface from cyclic voltammetry (CV) and electrochemical impedance spectroscopy (EIS) studies. The electrode's efficient sculpturing of stripes 0.2 mm in width was confirmed with electrochemical microscopy (SECM). Finally, by using X-ray photoelectron spectroscopy (XPS) and Raman spectroscopy, we confirmed no significant oxidation of the CB filler after FSL treatment. We revealed significant differences with ablation by longer nanosecond laser pulses, where significant heat transferred to the electrode surface contributed to partial melting and re-solidification of the PLA, negatively influencing the activation efficiency.

1. Introduction

3D printing technology has found numerous applications in everyday life, offering easy access to printing various shapes and objects at home cheaply and straightforwardly, as well as different industry branches, such as automotive [1], aviation [2], and space [3]. The creation of new 3D printable materials is performed in medicine, where antibacterial [4] or biocompatible filaments are printed to replace human bones [5], tissues, and organs [6]. Commercially available filaments from thermoplastic polymers with electrically conductive fillers are available for 3D printing and have been used in electronics to build simple temperature, stress, and touch sensors [7]. Thus, a rapidly developing trend is to create new materials for 3D printing with better mechanical and functional properties, and conductivity [8–10].

Fused deposition modelling (FDM) is the most popular amongst 3D printing technologies [11]. It is a type of additive manufacturing technology in which the material filament is introduced from spools through an extruder into a pre-heated printer head, where the polymer becomes semi-liquid. The filament is pressed out by the head and distributed on the worktable, layer-by-layer, forming a three-dimensional object [12]. The technology offers the unique opportunity of printing simple free-standing structures, where different electrically conductive carbon fillers are currently being investigated for their suitability in electrochemistry. The cost of producing a single electrode in this technology is meagre, offering an attractive alternative to more demanding electrode materials in electrochemical research. The available literature includes the use of 3D printed electrodes as energy storage devices [13–16], and in electroanalysis, where the detection of compounds such as ascorbic and picric acid [17], Pb^{2+} and Cd^{2+} ions [18,19], TNT [20], dopamine [21], caffeine [22] and H_2O_2 [11] were reported. The most commonly studied polymer in this regard is polylactic acid (PLA).

The use of the PLA-based 3D prints in electroanalysis requires the removal of the polymer matrix and exposure of the conductive carbon filler. This operation activates the surface, improving (or, in some cases, providing) the electrochemical response. Only a few available studies [23–25] indicate the electrochemical activity of these electrode surfaces

* Corresponding author.
E-mail address: jacek.ryl@pg.edu.pl (J. Ryl).

https://doi.org/10.1016/j.electacta.2022.140288
Received 29 November 2021; Received in revised form 11 February 2022; Accepted 27 March 2022
Available online 28 March 2022

immediately after the printing process. Here, one should consider the limited transfer efficiency at the electrode/electrolyte interface and the type of the redox probe used, varying in the charge transfer mechanism. The process is further influenced by different conductive carbon filler types, such as graphene [17], carbon black [26], or carbon nanotubes [27].

Surface activation can be carried out by immersing the electrode in an aprotic solvent [28,29], where the best results are obtained for dimethylformamide [17,30,31]. Different activation routes include electrolysis in aqueous electrolytes [32], and enzymolysis in proteinase K [26,33]. In a previous work, our group focused on a new surface activation protocol of CB-PLA electrodes by laser ablation [22]. A Nd:YAG laser was used for this process. After optimising the process parameters, we have reported that the laser ablation process effectively removes the polymer matrix from the CB-PLA electrodes' surfaces, significantly enhancing the kinetics of the redox process and the available electrochemically active surface area (EASA). In addition, the activation protocol is time-efficient and does not require the use of toxic chemicals.

On the other hand, nanosecond laser treatment may lead to undesirable, thermally induced surface effects, such as changes in the composition, or carbonisation, or melting and resolidification of the material [34,35], and generate active sites when using filament fillers for electrocatalysis [36]. Here, femtosecond laser (FSL) offers significant advantages, allowing precise ablation with zero or negligible thermal influence on the surrounding material [37]. FSL ablation may thus constitute a promising approach to micro- and nanostructurisation of 3D printouts. Laser pulses allow high-density energy to be deposited into the material in a short time, thereby minimising thermal effects on the surface during the ablation process [35]. Due to its unique processing properties, FSL has wide application in many fields, such as materials processing [38,39], and microcomponents production [40,41]. In their work, Kanasaki et al. [42] observed that the excitation of graphite with FSL leads to the appearance of sp^3-carbon nanodomains. The characterised structure differed thermodynamically from conventionally formed diamond and may correspond to a new carbon structure. Saikiran et al. used FSL to produce nanogratings on a bulk graphite surface in air and to create various carbon nanostructures such as graphene quantum dots, nano graphitic sheets, and few-layered graphene, by straightforward, single-step FSL irradiation of the graphite surface in water [43]. Ultra-short laser pulses were studied by Moreno et al. [44] to assess the influence on microstructuring of polymer composites with carbon fillers. It was found that the polymers exhibit different behaviour depending on whether the filler is carbon black or carbon fibres. The FSL processing gave rise to high-quality structures for carbon black, while the energy was absorbed in the case of the fibres and transferred to the surrounding polymer, resulting in sub-optimal effects, such as waviness and irregular shapes. Moreover, the changes observed in materials subjected to laser micromachining can be characteristic of both pico- and femtosecond interactions.

In light of the above reports, our goal was to evaluate how FSL used as the ablation source for CB-PLA 3D printout surface activation affects the charge transfer kinetics. Furthermore, FSL offers strict and precise local control of the ablated surface area, providing the unique opportunity to study the possibility of local surface activation. The locally-activated surface can be further used for locally-sculptured surface functionalisation, i.e. electrodeposition. Thus, to the best of our knowledge, we present the first study of tailoring micropatterns with different electrochemical characteristics at the surface of 3D-printed electrodes. The electrochemical and physicochemical characteristics of the CB-PLA electrodes obtained as a result of Nd:YAG and FSL ablation were compared.

2. Experimental

2.1. Electrode material

The filament material for 3D printed electrodes was commercially available Proto-Pasta Conductive PLA. It contains 26.4 wt.% of carbon black filler, which results in 30 Ω•m of electric resistivity [22]. Flat electrodes with dimensions of 11×11×2 mm, were printed on a Zmorph Fab (Zmorph, Poland). The 3D printing process parameters were as follows: printing temperature 210 °C, bed temperature 60 °C, layer height 0.2 mm, nozzle diameter 0.4 mm, printing speed of the two first and two last layers 20 mm/s, printing speed for the middle layers 40 mm/s, infill density 100%, and extrusion multiplier 1.1. The electrode designs were sketched in 123D Design (Autodesk, Inc., USA) and sliced with the Voxelizer software (Zmorph, Poland) which is dedicated for Zmorph printers.

2.2. Laser ablation

The laser processing of the 3D-printed CB-PLA electrodes was carried out by means of two lasers: Nd:YAG (neodymium-doped yttrium aluminium garnet) operating at 1064 nm with 8 ns pulse duration (LaserBlast 500, Quantel, France) and an FSL operating at 1030 nm with 356 fs pulse duration (ORIGAMI XP, NKT Photonics, Denmark). The Nd:YAG laser was equipped with diffractive optics delivering a top-hat beam profile and square laser spot. The samples were scanned with a spot of 5×5 mm^2 while the energy density on the sample surface was set to 0.64 J cm^{-2}. The laser pulse repetition was set to 2 Hz to avoid thermal effects on the sample. The best results were obtained with these parameters, as presented in our previous work [22]. In turn, the FSL delivered a Gaussian beam with pulse energy between 4 μJ and 44.4 μJ depending on the pulse repetition rate adjustable from 1 MHz to 50 kHz, respectively. In the case of the current research, the pulse frequency was set to 200 kHz corresponding to a maximal pulse energy of 20.1 μJ. The laser beam was focused on the sample surface to a spot of 25 μm diameter and the sample surface was scanned by means of an XY galvanometer scanner. The samples were processed in an air atmosphere. The number of laser pulses per one point, resulting from the scan rate (833, 1000, or 2500 mm/s) as well as the laser energy (see **Table 1**), were tuned individually to obtain the desired processing parameters.

It can be seen that, although the values of energy density on the sample surface (E_i/S) do not differ much between both lasers, there is a significant difference (5 orders of magnitude) in the power density (P_i/S) resulting from a combination of differences in parameters such as the laser pulse duration (t_i), repetition rate (f) and energy (E_i) as well as the surface area of the laser spot on the sample (S).

2.3. Electrochemical measurements

The electrochemical measurements were carried out in the three electrode setup system with the CB-PLA as the working electrode, Ag|AgCl (3 M KCl) as the reference electrode, and a Pt mesh as the counter electrode after initial conditioning for 10 min. Electrochemical impedance spectroscopy (EIS) and cyclic voltammetry (CV) were performed on a Gamry Reference 600+ potentiostat (Gamry Instruments) in a 5 mL electrochemical cell in a naturally aerated solution.

The diameter of the electrochemical cell was 0.8 cm, which corresponds to a 0.503 cm^2 geometrical area of the tested electrodes. To assess the effect of locally-sculptured modification of the electrode surface area, only a fraction X of the surface area exposed to the electrolyte and subjected to electrochemical tests was laser-ablated, where X was equal to 0% (reference), 10%, 25%, 50%, 75%, 90% or 100%. For the Nd:YAG laser, it was impossible to directly activate only a small portion of the electrode surface area. Thus, masks were put over the top of the 3D printed CB-PLA, with the X fraction exposed, as presented in **Scheme 1**.

Table 1
Differences in lasers and parameters.

Laser	t_i / fs	F / Hz	$T=1/f$ / s	E_i / μJ	P_i / W	S / cm^2	E_i/S / J cm^{-2}	P_i/S / W cm^{-2}	Label
FSL	356	$2\bullet10^5$	$5\bullet10^{-5}$	20.1	$5.6\bullet10^7$	$4.9\bullet10^{-6}$	4.1	$12\bullet10^{12}$	E100
				15.1	$4.2\bullet10^7$		3.1	$8.6\bullet10^{12}$	E75
				10.1	$2.8\bullet10^7$		2.1	$5.8\bullet10^{12}$	E50
				5.0	$1.4\bullet10^7$		1.0	$2.9\bullet10^{12}$	E25
				2.0	$5.6\bullet10^6$		0.4	$1.2\bullet10^{12}$	E10
Nd:YAG	$8\bullet10^6$	2	0.5	$1.7\bullet10^5$	$2.1\bullet10^7$	0.26	0.64	$8\bullet10^7$	Nd:YAG

where: t_i – laser pulse duration, f – pulse repetition rate, T – period (time between two pulses), E_i – pulse energy, P_i – pulse power, S – surface area of the laser spot on the sample

The CV scans were conducted in two different solutions. The 1 mM hexaammineruthenium ($[Ru(NH_3)_6]^{2+}$) in 0.1 M KCl solution was used to determine the EASA. The scan rates were performed between 5 and 800 mV s^{-1} and in the polarisation range from −0.6 to 0.2 V vs Ag|AgCl. The hexacyanoferrate system (1.25 mM $[Fe(CN)_6]^{4-}$ + 1.25 mM $[Fe(CN)_6]^{3-}$ in 0.1 M KCl) solution was used to determine the optimal laser parameters because of its inner sphere electron transfer mechanism (see **Supplementary Information file, Section S1**). The EIS studies were tested with elementary perturbation signals in the frequency range from 10 kHz to 0.3 Hz, with 10 perturbation signals per frequency decade. The amplitude of the perturbation signal was 14 mV, and the measurements were carried out in potentiostatic mode after 10 min conditioning to reach the open circuit potential conditions. The EIS study was performed in the same two different electrolytes for a better understanding of the reaction kinetics.

Imaging of electrochemical activity was performed with a custom-built scanning electrochemical microscope (SECM) composed of an Ivium CompactStat potentiostat and a mechOnics 3D micropositioning system. The SECM system was controlled and operated through the SECMx software [45]. A 100 μm diameter inlaid disk Pt microelectrode, acting as the SECM tip (working electrode), was obtained by sealing a 0.1 mm diameter Pt wire (Mint of Poland) into borosilicate glass capillaries using a PC-10 micropipette puller (Narishige) according to the procedure described elsewhere [46]. A 0.5 mm diameter Pt wire and Ag|AgCl|KCl(3 M) were used as the counter and reference electrodes, respectively. The sample with laser-ablated lines was mounted in the bottom of a custom-made Teflon SECM cell so that the SECM scanning area covered both the ablated lines and the intact sample surface. Constant height imaging was performed with the unbiased sample in 0.8 mM of ferrocenemethanol containing 0.1 M KCl as a supporting electrolyte. The tip was polarised at +0.5 V vs. Ag|AgCl to assure diffusion-limited electrooxidation of the ferrocenemethanol. The tip-to-sample distance was adjusted to 50 μm (normalised distance $d/r_T = 1$).

2.4. Physico-chemical characterisation

A FEI Quanta 250 FEG (ThermoFisher Scientific) equipped with a Schottky field emission gun was used to acquire scanning electron microscopy (SEM) micrographs. The microscope was operating with secondary electrons, under a 20 kV accelerating voltage and in high vacuum mode.

High-resolution X-ray photoelectron spectroscopy (XPS) spectra were recorded with an Escalab 250Xi multispectroscope (ThermoFisher Scientific). The spectroscope was operating with an AlKα X-ray source, and a spot size of 650 μm. The spectra were collected in the C1s and O1s binding energy range, with a 20 eV pass energy. The flood gun emitting low-energy electrons and low-energy Ar^+ ions served for charge compensation, with final spectra calibration for adventitious carbon (C1s at 284.8 eV).

A Raman analysis was performed using a Raman microscope (InVia, Renishaw, UK). Spectra were recorded in the range of 150–3200 cm^{-1} using an argon-ion laser emitting at 514.5 nm and operating at 1% of its total power (50 mW) to avoid melting the PLA. Each sample was analysed at five randomly selected points on its surface using a 50x objective lens microscope. The spectrum of each point on the samples were recorded as an accumulation of five scans. Each sample was analysed in the area irradiated with the laser, and reference measurements for each sample were recorded from the untreated surface.

A 3D reconstruction of the topography of the sample with the laser-ablated stripe (**Fig. 6c**) was recorded with a Nikon Ti2-U inverted optical microscope equipped with a Hamamatsu ORCA 4 v3 greyscale camera and CFI Plan Fluor 10x objective (NA = 0.3). The topography image was obtained by stacking the sharpest regions of a series of images recorded at different vertical positions of the objective versus the sample using dedicated Nikon NIS AR software.

3. Results and discussion

3.1. Topography and structural modification by the femtosecond laser ablation

The EIS and CV results obtained for different FSL energies are shown in **Fig. 1**. The optimisation study of other tested parameters was less significant and is presented in the **Supplementary Information file, Section S1**. The minimum proposed laser energy equal to 2 μJ (E10) was appropriately increased. For the CV scans (**Fig. 1a**), the untreated CB-PLA electrode did not show $[Ru(NH_3)_6]^{2+/3+}$ oxidation/reduction peaks, manifesting a restricted, irreversible charge transfer process. The increase of the electrochemical response is visible even for the minimum FSL energy and further rises with the increasing laser energy. The best results were obtained at the highest pulse energies for samples E75 and E100. For each study, the peak-to-peak ΔE value equals 128.1 mV and 96.2 mV, decreasing with the laser energy increase and indicating a quasi-reversible character of the electron transfer. The ΔE parameter allows for estimation of the heterogeneous rate constant, k^0, which was done using the Nicholson approach [47,48], see Eq. (1).

$$k^0 = \Psi\left(\pi D_0 \frac{nFv}{RT}\right)^{1/2} \quad (1)$$

where ψ is the dimensionless kinetic parameter estimated from the literature based on peak potential separation ΔE [47], D_0 is the diffusion coefficient ($9.10\bullet10^{-6}$ cm^2 s^{-1}), n is the number of electrons transferred, υ is the applied scan rate (100 mV s^{-1}), R is the gas constant, F is the Faradaic constant and T is the temperature. The results (see **Table 2**) suggest that the FSL energy influences the heterogeneous rate constant, increasing it to some extent. On the other hand, the simultaneously observed increase in the redox probe peak currents (I_a, I_c) suggests EASA development with the FSL energy increase. It appears that the laser ablation is optimal if the E_i is not less than 15.1 μJ. Compared to Nd:YAG ablation, the FSL seems to offer comparable yet slightly smaller EASA development, with significantly higher rate constants. On the other hand, for the untreated CB-PLA electrodes, the electrochemical response is practically invisible.

The EIS measurements are another tool to verify the optimal FSL energy used. The obtained EIS results are summarised in **Fig. 1b**. It can be seen that the spectra of each ablated CB-PLA sample are composed of

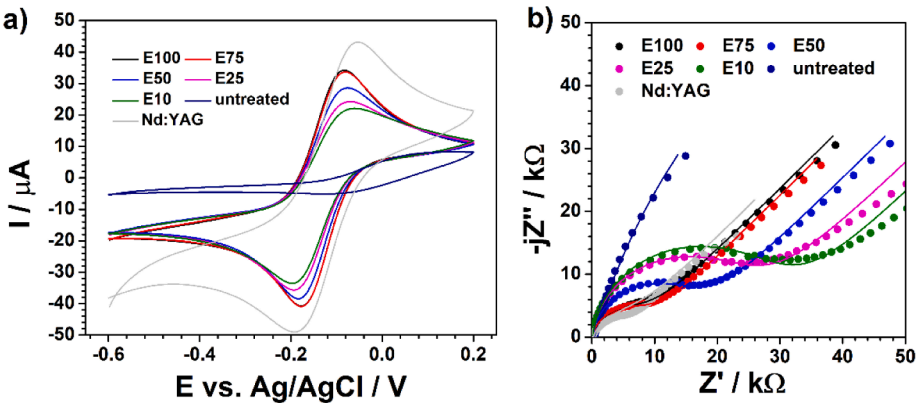

Fig. 1. (a) CV scans (at 100 mV s^{-1}) and (b) EIS spectra in the Nyquist projection for Nd:YAG and FSL ablation, the latter with different energies used. In EIS spectra, the points mark experimental results, the solid line the EEC fitting. The redox probe was 1 mM $[Ru(NH_3)_6]^{2+}$ in 0.1 M KCl.

Table 2
CV and EIS spectra parameters estimated for CB-PLA electrodes treated by FSL under different ablation energies and Nd:YAG, EIS analysis based on the discussed EEC's.

Parameter	FSL-abated						Nd:YAG
	E100	E75	E50	E25	E10	Untreated	ablated
ΔE / mV	92	97	105	121	136	-	138
I_a / µA	34.24	33.68	28.61	24.28	22.08	-	43.18
k^0 / cm s^{-1}	$7.98•10^{-3}$	$5.32•10^{-3}$	$5.32•10^{-3}$	$3.72•10^{-3}$	$2.66•10^{-3}$	-	$2.66•10^{-3}$
Q / µF $s^{\alpha-1}$	0.36	0.30	0.20	0.16	0.15	19.6	1.97
α / -	0.92	0.92	0.94	0.95	0.93	0.82	0.82
R_{CT} / kΩ	7.84	8.47	15.93	24.13	28.87	199.95	7.41
W / µS $s^{1/2}$	17.3	19.5	17.4	14.7	16.2	-	25.1

a single capacitive time constant at a mid-to-high frequency range and with characteristic 45° tail in the low-frequency range, representing diffusion through a semi-infinite medium. The diameter of the semi-circle loop decreases with the increased FSL energy, indicating the decrease of charge transfer resistance and thus confirming previously obtained conclusions. However, to perform a detailed spectral analysis, one needs to carry the fitting procedure with the equivalent electric circuit (EEC), representing the electric parameters at the electrolyte/electrode interface. The EEC selected for this purpose was a modified Randles circuit, R_e(CPE(R_{CT}W)), with a constant phase element (CPE) instead of a capacitor to properly consider the electric and geometrical heterogeneities of the studied CB-PLA electrode [48]. Here, R_e stands for the series resistance, primarily attributed to the electrolyte resistance, while R_{CT} represents the charge transfer resistance through the interface. The CPE impedance is given by Eq. (2) [49]

$$Z_{CPE} = [Q(j\omega)^{\alpha}]^{-1} \quad (2)$$

and represented by two parameters, *quasi*-capacitance of the electrical double layer Q, and CPE exponent α. For α = 1, the CPE describes the ideal capacitor behaviour; thus, it is often called the heterogeneity factor. Finally, Warburg element W models the diffusion process. A simplified R_e(CPE-R_{CT}) EEC was used for the reference, untreated sample only, where the diffusion tail was not seen in the studied frequency range due to the hindered electrode kinetics and irreversibility of the charge transfer process. The fitting procedure results are summarised in **Table 2**, and the fit quality is visualised as a solid line in **Fig. 1**.

The R_{CT} decrease with the FSL energy increase is noticeable, confirming its importance during CB-PLA surface activation by laser ablation. Similar to peak current i_p in the CV results, the highest electrode response is obtained for the E75 and E100 samples, with R_{CT} decreasing by over an order of magnitude compared to the reference, untreated sample. A consecutive increase in quasi-capacitance Q assists in changes in the R_{CT} values. This character is to be expected and should be explained with notable differences in the EASA values and the EASA increase with the FSL energy according to Eq. (3).

$$C = \frac{\varepsilon_0 \varepsilon A}{d} \quad (3)$$

where ε^0 and ε represent the permittivity and dielectric constant, respectively, A is the surface area (EASA), and d is the electrical double layer thickness. On the other hand, the results obtained for the CB-PLA after Nd:YAG ablation reveal R_{CT} to be nearly identical as in the case of the FSL-ablated E100 sample. At the same time, the Nd:YAG-processed sample shows significantly higher *quasi*-capacitance Q, which hints toward altered charge accumulation and transfer within the electric double layer.

The SEM study of the topography of the FSL-ablated CB-PLA electrodes confirms the origin of the altered electrochemical response when treated with different laser energies E_i, as visualised in **Fig. 2**. It becomes clear that operating at insufficiently low energies, the PLA matrix does not evaporate during the treatment duration, as seen for E_i equal to 2 and 5 µJ (**Fig. 2a** and **2b**, respectively). The PLA covers the CB nanoparticles, and only higher FSL energies allow their effective exposure, thus increasing the electrochemically active surface area available for the redox process.

Next, the high-resolution XPS analyses were performed for the CB-PLA samples ablated at different FLS energies and compared with Nd:YAG surface processing. The C1s and O1s spectra are presented in **Fig. 3a** and **3b**, respectively.

The XPS spectra were deconvoluted for in-depth analysis of the surface changes resulting from FSL ablation. The C1s spectra shape (**Fig. 3a**) suggests complex carbon chemistry with at least four different components, partially overlapping. The primary C_1 peak was recorded at approx. 283.7 eV and ascribed to the CB nanoparticle filler in the PLA matrix. The following three components, C_2–C_4, are characteristic of the chemical bonds present in the poly(lactic acid). The signal peaking at 284.8 eV is common for C-C aliphatic bonds, while C_3 and C_4 are peaking at the binding energies most often ascribed to C-O and C=O bonds, respectively [50]. The theoretical C_2:C_3:C_4 ratio in PLA should be 1:1:1, yet a slightly higher C_2 share is expected due to the adventitious carbon

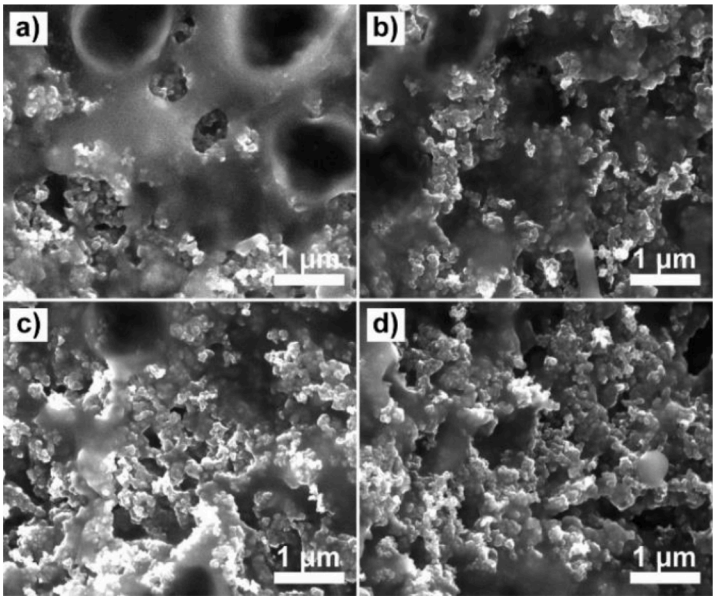

Fig. 2. SEM micrographs of the 3D-printed G-PLA electrode topography after surface modification with femtosecond laser under different ablation energies E_i, i.e.: (a) E10, (b) E25, (c) E50, (d) E100. Samples labels are explained in Table 1.

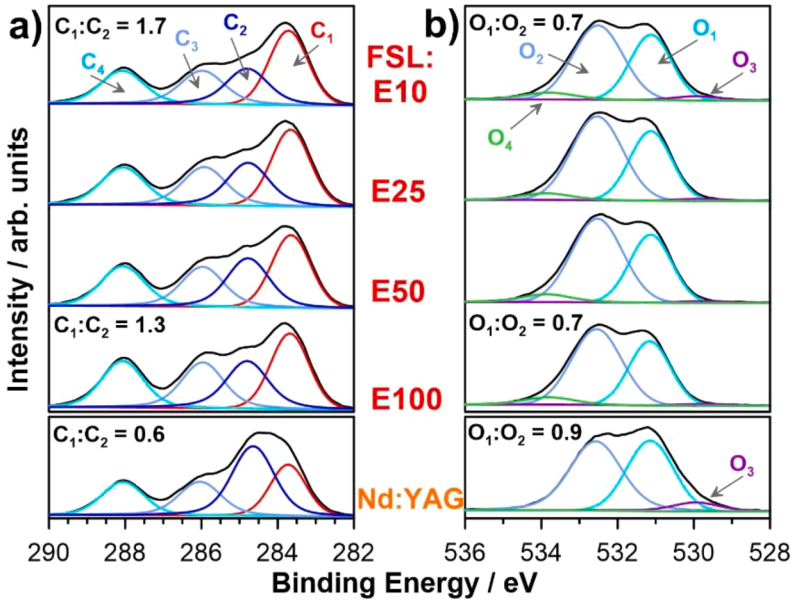

Fig. 3. High-resolution XPS spectra recorded for FSL-ablated CB-PLA samples E10, E25, E50, E100 and Nd:YAG-ablated CB-PLA sample in the core-level binding energy range of (a) C1s and (b) O1s, with peak deconvolution.

contamination from atmospheric air exposure [51].

On the other hand, the O1s spectra consist of two main components, ascribed to C=O (O_1 at 531.1 eV) and C-O (O_2 at 532.5 eV) bonds within the PLA matrix. Two minor features were noted: the first, O_3, at low binding energies, represents metal oxide contamination during filament fabrication [52], and the latter, O_4, due to the presence of chemisorbed water molecules [53]. The results of the deconvolution are summarised in **Table 3**.

It appears that increasing the FSL energy during the ablation leads to a slight but progressive decrease in the C_1 component share, from 27.2 to 22.1 at.% between the E10 and E100 samples. An increase in the C_2 species share assists this trend, while C_3 and C_4 appear to be unaffected. Similar behaviour was previously observed for various activation treatments [22,26] and connected to partial oxidation of the CB

Table 3
FSL and Nd:YAG-ablated CB-PLA surface chemical composition based on high-resolution XPS spectra, deconvoluted using the proposed fitting model.

Deconvoluted peak			BE / eV	FSL-ablated				Nd:YAG
				E10	E25	E50	E100	ablated
C1s	C_1	sp^2-C	283.7	27.2	25.5	23.2	22.1	16.9
	C_2	C-C	284.8	16.0	17.3	18.4	17.3	28.2
	C_3	C-O	286.0	15.4	15.7	15.6	16.2	13.8
	C_4	C=O	288.1	14.3	14.8	15.2	15.6	12.7
O1s	O_1	C=O	531.1	10.4	10.0	10.2	11.0	12.3
	O_2	C-O	532.5	14.3	14.9	15.4	15.8	14.4
	O_3	Me-O	529.9	0.9	0.5	0.4	0.5	1.8
	O_4	H_2O	533.8	1.4	1.4	1.6	1.5	–

nanoparticle filler and/or rapid surface area development under laser treatment with consecutive adventitious carbon adsorption. Thus, the most apparent C_1:C_2 shift, which is observed for Nd:YAG ablation, may suggest CB filler oxidation by the nanosecond laser. A notable increase in O_1 share after Nd:YAG treatment suggests carbonyl species formation at the electrode surface. These results corroborate earlier discussed changes in rate constant k^0 and *quasi*-capacitance Q. On the other hand, under the FSL treatment, the oxygen chemistry is nearly unaffected, regardless of the ablation happening in an air atmosphere, with the O_1:O_2 ratio remaining at 0.7:1 for each studied laser power. Moreover, the increase in total [O] was negligible, only reaching 1.8 at.%. In our previous reports and other ablation studies in O_2 plasma [54], changes in oxygen chemistry were more prominent.

It appears that unlike the work of Kanasaki et al. [42], the FSL action did not result in the transformation of CB, forming sp^3-carbon nanodomains, as it would have shifted the primary C1s component towards higher binding energies. Moreover, it should be noted that as a result of the FSL ablation, regardless of laser power, the C_2:C_3:C_4 ratio is much closer to that expected for poly(lactic acid), compared with the Nd:YAG laser (28.2:13.8:12.7), where the C_2 component was twice the share of the C_3 and C_4 features [22]. This effect is most possibly related to the combustion of the adventitious carbon under FSL action and will be discussed further. Overall, the FSL ablation did not lead to significant structural differences. On the other hand, the surface chemistry alteration was the most negligible amongst the reports available to date.

Both the SEM and XPS analyses explained the electrochemical findings, concluding that FSL ablation primarily affects the EASA uncovering the CB nanoparticles and is highly laser energy-dependant. Changes in charge transfer kinetics are negligible as the CB chemistry is most likely unaffected throughout the process.

3.2. Efficiency of area-localised CB-PLA surface activation

After selecting the optimal FSL operating parameters (E100: E_i = 20.1 μJ, v = 2500 mm s^{-1}, single scan), the next step was to evaluate the efficacy of the localised CB-PLA electrode surface ablation and electrochemical activation of locally-sculptured specific areas. We decided to ablate circular areas at the CB-PLA surface, ranging between 10 and 100% of the total surface area exposed to the electrolyte. The idea of this experiment is schematically presented in Fig. 4**a**. The red spot in the middle of the studied CB-PLA electrode surface is an FSL ablated surface area, while the rest of the electrode was untreated. The EIS measurements were carried out in the presence of two different redox probes, i.e. $[Ru(NH_3)_6]^{2+/3+}$ (Fig. 4**a**) and $[Fe(CN)_6]^{3-/4-}$ (Fig. 4**b**), which made it possible to examine the effect of the electron transfer mechanism using the redox probe.

There is a significant difference in the shape and size of the surface-treated CB-PLA electrodes depending on the redox probe used, regardless of the share of the locally ablated surface area. Notably, in the hexacyanoferrate system, the low-frequency impedance response is heavily affected, introducing an artificial spectral shape. Thus, to reduce the level of the fitting error, we decided to restrict the studied frequency range up to 1.77 Hz (red and blue arrows in Fig. 4**b** mark 1.77 Hz for laser ablated electrode share of 25% and 50%, respectively) and utilise R_e(CPE-R_{CT}) EEC. For the hexaammineruthenium system, the EEC was R_e(CPE(R_{CT}W)). The EIS analysis results are presented in Table 4.

As a general trend, the expected outcome was achieved – the higher the FSL-modified surface area, the lower the charge transfer resistance R_{CT}; however, the observed changes had a significantly more random character when $[Fe(CN)_6]^{3-/4-}$ was used as the redox probe. Here, activation of 10% of the electrode surface resulted in a two-times R_{CT} decrease compared to an untreated electrode, and a further four-times drop when the ablated area share was 25%. However, when comparing between 10%- and 100%-modified electrodes, one order of magnitude of R_{CT} difference was preserved. A similar result was obtained for $[Ru(NH_3)_6]^{2+/3+}$. Here, however, the R_{CT} changes were more representative of the actual changes in the share of the electrochemically-activated CB-PLA surface. These data are visualized in **Supplementary Information file, Section S2.**

Such a difference between both probes is expected. Hexaammineruthenium has the outer sphere electron transfer (OSET) mechanism and does not require direct contact before or during the electron transfer event [55]. On the other hand, commonly used hexacyanoferrates are characterised by the inner sphere electron transfer (ISET) mechanism, thus requiring a covalent bond to be formed at the electrode surface [56]. The necessity of such adsorption makes the ISET probes significantly more reliant on the subtle changes in surface chemistry, the

Table 4
EIS spectra parameters calculated for CB-PLA electrodes with different FSL-ablated electrode shares, based on the studies with $[Ru(NH_3)_6]^{2+/3+}$ and $[Fe(CN)_6]^{3-/4-}$ redox probes.

Parameter	Laser ablated electrode share					
	100%	90%	75%	50%	25%	10%
Redox probe	1 mM $[Ru(NH_3)_6]^{2+/3+}$					
Q / μF$s^{\alpha-1}$	1.56	1.56	1.48	0.96	0.98	0.13
α / -	0.83	0.81	0.80	0.79	0.79	0.94
R_{ct} / kΩ	5.80	4.74	6.25	9.08	28.86	49.18
W / μS$s^{1/2}$	37.8	38.1	31.8	23.6	13.1	-
Redox probe	2.5 mM $[Fe(CN)_6]^{3-/4-}$					
Q / μF$s^{\alpha-1}$	0.29	0.28	0.22	0.19	0.15	0.16
α / -	0.95	0.95	0.95	0.96	0.96	0.93
R_{ct} / kΩ	12.92	13.25	18.97	18.04	23.26	94.25

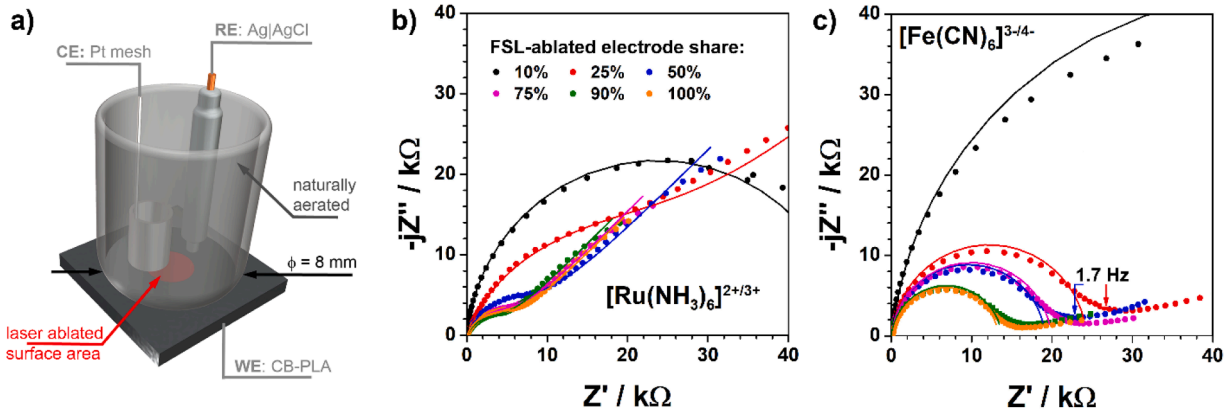

Fig. 4. (a) The scheme of the electrochemical cell used for the measurements, with FSL-ablated area marked in red; (b,c) EIS Nyquist plots of CB-PLA with different FSL-ablated electrode shares between 10 and 100%, studies in the presence of (b) 1 mM $[Ru(NH_3)_6]^{2+/3+}$ and c) 2.5 mM $[Fe(CN)_6]^{3-/4-}$. Laser ablation parameters for E100 sample: E_i = 20.1 μJ, v = 2500 mm s^{-1}, 1 scan.

electrode modification history, etc. The discussed difference is why the R_{CT} values in the presence of $[Ru(NH_3)_6]^{2+/3+}$ are always lower than for $[Fe(CN)_6]^{3-/4-}$, and more representative of the introduced EASA changes. The difference between the ISET and OSET redox probes is further visible in the case of the *quasi*-capacitance changes, where only OSET probes reveal some Q linearity with the FSL-ablated electrode share.

The CV studies in a wide scan rate (υ) range may shed some light on the exact values of the EASA and compare them to the shares of FSL-ablated CB-PLA electrode surfaces. The polarisation curves recorded for two different FSL-ablated surfaces, i.e. 25% and 90%, are shown in **Fig. 5a** and **5b**, respectively. It can be observed that the i_p value increases significantly between different areas of locally activated CB-PLA surfaces, testifying to the EASA development. The kinetics of the redox process (represented by ΔE and k^0) are also affected, as seen in **Supplementary Information file, Section S3**. The effective EASA estimation is based on the modified version of the Randles-Sevcik equation (Eq. (4)), for non-reversible one-step, one-electron reaction [57,58].

$$i_p = 2.99{\cdot}10^5 \alpha_*^{1/2} A C_O D_O^{1/2} \upsilon^{1/2} \quad (4)$$

where υ is the scan rate in V s^{-1}, α_* is the transfer coefficient, assumed as 0.5, A is the EASA, D_O is the diffusion coefficient of the redox probe oxidised form ($D_O = 9.10{\cdot}10^{-6}$ cm^2 s^{-1} for $[Ru(NH_3)_6]^{3+}$ [22]), and C_O is the redox probe concentration in mol cm^{-3}. The $i_p = f(\upsilon^{1/2})$ characteristics of each studied FSL-ablated surface share are presented in **Fig. 5c**.

The relationship given in **Fig. 5c** allowed the EASA to be estimated using Eq. (4). The calculated EASA values are plotted versus the FSL-ablated surface area in **Fig. 5d**. Using the peak current equation for an irreversible linear diffusion system, we only used data for $\upsilon^{1/2} > 0.25$. In the case of a heterogeneous electrode surface area, the diffusion profiles of the electrode reaction are partially overlapping, in particular at low scan rates, thus consequently lowering the recorded currents. The graph presented in **Fig. 5d** makes it possible to extract the relevant information regarding the efficiency of locally-sculptured CB-PLA surface activation by FSL. Most notably, there is a linear relationship between both of these parameters in a wide range of surface activation areas. Moreover, within this range, the EASA is approximately 2.5 times smaller than the FSL-ablated surface area, which suggests that activation efficiency by FSL is lower compared to the most efficient activation procedure reported, i.e. electrolysis in an alkaline media [26], where the EASA was nearly equal to the geometric surface area.

Only in the boundary conditions, when the FSL-ablated area of the CB-PLA samples was equal to a 10% and 90% share of the electrolyte-exposed surface area, a deviation from the linearity of the discussed relationship is visible. The sample at 90% of the FSL-ablated electrode area highly resembles the one with full surface activation. The resemblance between these electrodes holds regardless of the CV scan rate and is preserved in the EIS studies (see **Table 4**), and may result from the sample fixing in the electrochemical cell (see **Fig. 4a**). The FSL-ablated surface area for the 90% sample was a circle with a diameter of 7.58 mm, while the electrochemical cell had a diameter of 8.00 mm, leaving only approx. 5 mm^2 of the unactivated electrode area. On the other hand, the FSL-ablated circle for the 10% sample had a diameter of 2.5 mm, thus suggesting the presence of boundary effects, breaking the linearity of the above-discussed characteristics.

In order to evaluate the charge transfer differentiation at the boundary between the FSL-ablated and unactivated surface areas as well as the spatial resolution of the proposed treatment, we performed the SECM measurements. The FSL ablation was performed in a 200 μm wide linescan. The SECM electrochemical activity maps are presented in **Fig. 6a and 6b**, together with the topographic profile of the structure in **Fig. 6c**.

A relatively large SECM tip (50 μm radius Pt disk) was selected for

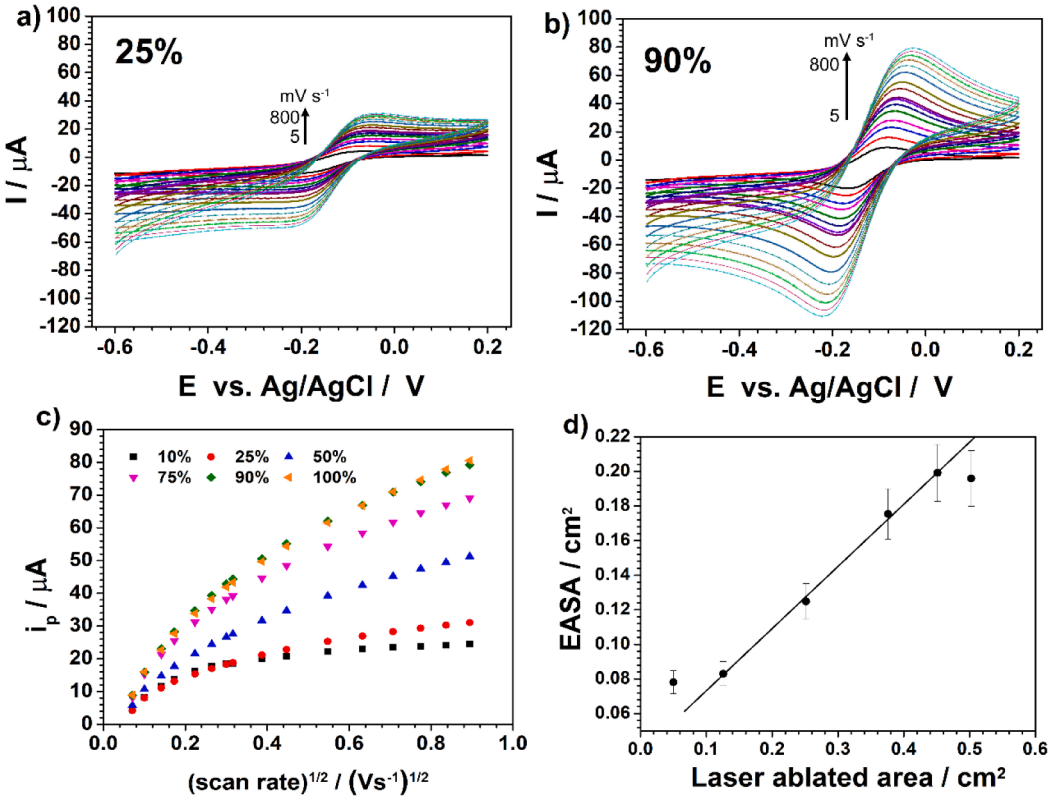

Fig. 5. (a,b) CVs at different scan rates for CB-PLA electrodes with FSL-ablated shares of 25% and 100% of the electrolyte-exposed surface, respectively, (c) peak current i_p vs scan rate square root $\upsilon^{1/2}$ relationship for different FSL-ablated electrodes, (d) resultant relationship between EASA and FSL-ablated electrode area. Electrolyte 1 mM $[Ru(NH_3)_6]^{2+/3+}$ in 0.1 M KCl. FSL ablation conditions: E100, ν = 2500 mm/s, 1 scan.

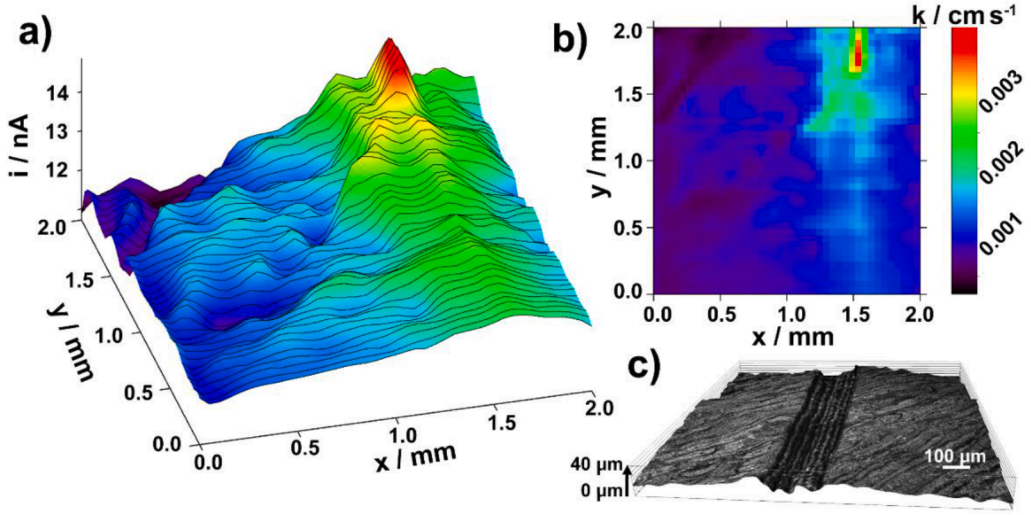

Fig. 6. (a) SECM image of FSL (E100) local ablation at CB-PLA surface recorded with a 100 µm diameter Pt disk microelectrode tip with (b) map of effective rate constant k_{eff} of ferrocenemethanol reduced form regeneration estimated from SECM image, and (c) topography map of the ablated surface. Electrolyte 0.8 mM ferrocenemethanol in 0.1 M KCl. Tip-to-sample distance: 50 µm. Scanning rate: 25 µm s^{-1} (50 µm from pixel to pixel with 1 s stabilisation before current sampling).

imaging the sample due to its intrinsic topography caused by the fabrication technology with FDM printing. The topography map in Fig. 6**c** reveals an average peak-to-peak roughness of the intact part of the sample as ~20 µm. The depth of the laser-ablated line is of a similar magnitude as the roughness (~20 µm). The results of constant height SECM imaging of such a sample with smaller microelectrode tips could be substantially affected by the sample topography since the signal at the SECM tip is a function of both the sample activity and the tip-to-sample distance. Constant height scanning with the SECM tip positioned above the sample at a distance the same as its radius (here 50 µm) obtains a decent contrast. For a sample with vertical topographic features shorter than the tip radius, the recorded current corresponds mainly to the local activity of the sample. The influence of the topography is minimised for a tip-to-sample distance as high as 50 µm for this particular sample. One can state that the SECM image in Fig. 6**a** represents mainly the distribution of electrochemical activity at the sample with little influence on its topography. Moreover, the tip current of 11.5 nA for the SECM tip positioned at a long distance from the sample (electrolyte bulk) was lower than when the tip was positioned close to the sample. This positive feedback confirms the regeneration of the mediator at the sample. A slightly recessed area of the laser-ablated line results in a bit longer tip-to-sample distance when scanning over this line in the constant height mode. Nevertheless, the current recorded at the tip positioned above the activated surface was higher. This confirms increased activity towards the regeneration of ferrocenemethanol at the stripe fabricated by laser ablation. It can be seen in the right part of the SECM micrograph parallel to the Y-axis in the image, centred around $X \approx 1.5$ mm. These results demonstrate local surface activation of the 3D-printed CB-PLA electrode for charge transfer processes by FSL ablation.

We also made an attempt to estimate the effective rate constant of regeneration of the ferrocenemethanol (reduction of its oxidised form, $FcMeOH^+$) in the scanned area. The map of this kinetic parameter (Fig. 6**b**) was calculated numerically from the current map using an equation from [59], with a rough assumption of a constant distance of 50 µm. The fastest kinetics corresponding to an activated area shows the effective rate constant of $k_{eff} = 3.6 \cdot 10^{-3}$ cm s^{-1}, whereas the lowest ($k_{eff} = 5 \cdot 10^{-4}$ cm s^{-1}) was detected on a pristine CB-PLA part. Laser activation can accelerate the electron transfer kinetics for ferrocenemethanol more than 7-fold.

While the FSL-ablated stripe was 200 µm in width, the SECM maps could suggest that the increased charge transfer kinetics also occurs in the vicinity of an approximately 500 µm stripe width. This effect is caused by the quite large size of the active part of the SECM tip (diameter 100 µm) and relatively long tip-to-sample distance (~50 µm). Both the distance and tip size affect the lateral resolution of feedback mode SECM imaging [60]. Notably, the electrochemical behaviour in the untreated electrode zone reveals a certain level of electric heterogeneity, as is expected, given that the CB nanoparticles are randomly located at different depths within the PLA matrix. The result explains the partial response of the untreated CB-PLA electrode.

The edge of the FSL-ablated stripe sculptured during sculptured linear activation is visualised in the SEM micrograph in Fig. 7**a**. At the same time, the laser-ablated and unaffected CB-PLA electrode surface areas are shown in Fig. 7**b** and 7**c**, respectively.

The micrograph reveals the repeatable topography features, and the remainder of the local FSL treatment. The boundary between both areas is approximately 50 µm wide; less than is seen on the SECM map. The laser treatment evaporates the PLA matrix, uncovering the CB nanoparticle clusters, as seen in Fig. 7**b**. However, the CB nanoparticles located directly under the surface are easily recognisable, including for the untreated CB-PLA surface (Fig. 7**c**), which explains the local heterogeneities in the electrochemical response, particularly when using outer sphere redox probes [23,25].

3.3. *Influence of thermal modification factor*

The efficiency of the ablation treatment with an Nd:YAG nanosecond laser was recently reported by us [22]. However, in the work mentioned above, we focused on determining the CB-PLA activation efficiency, allowing for the successful electroanalysis of organic compounds (caffeine). In light of the above-discussed results, it is interesting to evaluate whether the Nd:YAG laser also makes locally-sculptured and designed CB-PLA surface activation possible. However, to successfully restrict the ablation zone, masks were also 3D-printed to cover the CB-PLA electrodes throughout the laser treatment (see Scheme 1). As in the previous case, the uncovered electrode area X ranged from 10 to 100% of the total electrolyte-exposed surface area. The results of the electrochemical studies after local Nd:YAG laser treatment of the CB-PLA electrodes are summarised in Fig. 8.

The electrochemical response when tracking the hexaammineruthenium oxidation/reduction process was only noticeable at high percentages of Nd:YAG-activated CB-PLA surface areas, i.e., 75% and above (see Fig. 8**a–c**). The inefficiency of local surface activation of the smaller zones by Nd:YAG was the primary observed difference

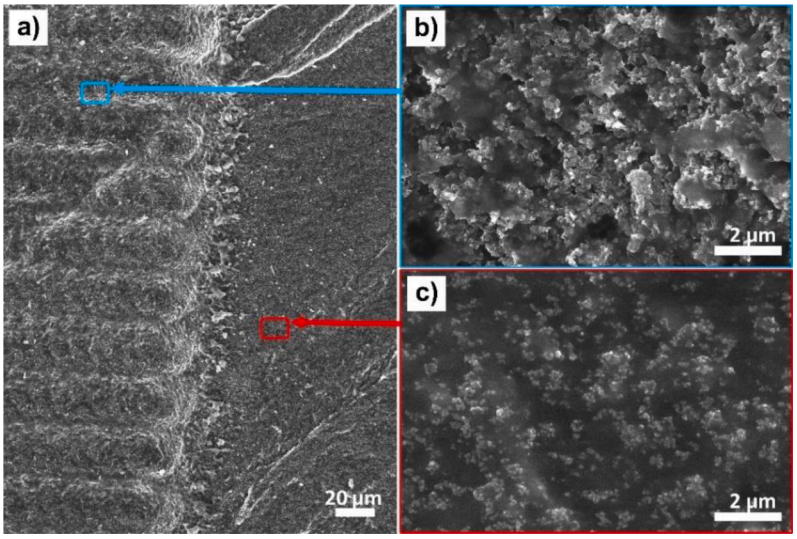

Fig. 7. (a) SEM micrographs of the G-PLA 3D-printed electrode, locally surface treated with femtosecond laser under optimised operating conditions, showing the boundary region between (b) laser-ablated and (c) unmodified G-PLA surface.

compared with FSL, where the electrochemical response was achieved even when only 10% of the electrode surface area was subjected to modification. The i_p vs scan rate square root $\upsilon^{1/2}$ function (Fig. 8**d**) reveals a similar trend as in the case of the FSL treatment (Fig. 5**d**), with deflection and loss of function linearity around the 80 mV s^{-1} scan rate range. Another important conclusion should be drawn when comparing the i_p values registered for the various laser-ablated electrode fractions. This is best observed based on the EASA characteristic changes shown in Fig. 8**e,** and estimated using Eq. (4). While the EASA still tends to increase with the fraction of the activated CB-PLA surface area, no linearity is visible, and the resultant electrode characteristics are more random. The EIS results support these conclusions (see Fig. 8**f**). The three electrodes with the lowest fraction of laser-ablated surface area present nearly identical impedance characteristics. A significant drop in the registered impedance values is only visible for samples at 75% of the Nd:YAG-ablated surface area and above.

When trying to identify the reason for the altered behaviour, we used the XPS (as already discussed in Section 3.1) and Raman spectroscopy studies. The Raman spectra recorded for both untreated (pristine) and FSL-processed CB-PLA electrode surfaces are presented in Fig. 9**a**.

The spectra are dominated by a D band centred at 1361 cm^{-1}, associated with disordered sp^3-hybridised carbon featured as defects or impurities in the carbon materials, and a G band centred at 1596 cm^{-1}, associated with the E2g phonon modes of the sp^2-bonded carbon. Both of the mentioned bands derive from carbon black filling [61,62]. Raman spectroscopy cannot provide direct information from the PLA matrix due to the big difference in laser radiation absorption and scattering coefficients in PLA and CB components. The most visible effect of laser processing of the electrode surface was the increase of background photoluminescence. This phenomenon, which originates from structural defects caused by thermal quenching and re-solidification [63,64], indicates degradation of the PLA during laser ablation in the presence of oxygen. The amount of fluorescence slightly differs depending on the laser used, and the background signal becomes more intense if the samples are processed with the FSL. This effect may be related to the dynamics of the thermal quenching and re-solidification processes, which are significantly different for the ns and fs laser pulses.

The energy densities of both lasers differ just within one order of magnitude. Yet, a significant difference in laser pulse duration (see Table 1) entails a huge difference in power densities, which in turn may have resulted in the generation of more surface defects in the polymer structure. The background-corrected spectra, shown in Fig. 8**b**, confirmed the results of XPS measurements that the laser treatment does not cause any modification of the chemical structure of CB nanoparticles. Likewise, the above-discussed XPS results allow it to be concluded that there was only slight variation in the CB-PLA surface chemistry depending on the laser used, with the FSL notably leading to a lower share of oxidised species present at the electrode surface.

The physics and mechanisms of the ablation process in the ultra-short pulse regime of the FSL are significantly different from those of nanosecond lasers, as the duration of the femtosecond laser pulse is shorter than the thermal relaxation time (on the order of 10^{-12} s). The ablation model specific to nanosecond and longer pulses is not applicable. The interaction of ultra-short pulse radiation with matter is very complex. It is necessary to consider that the processed materials' optical and thermodynamic properties change non-linearly under the influence of ultra-short laser pulses due to thermodynamic imbalance. The FSL pulses of high intensity are absorbed by electrons in a thin layer of material, leading to rapid ionisation [65]. At the end of the pulse, phonons are emitted during the relaxation of the electrons, and their temperature increases rapidly, approaching critical. The material is then in an unstable and unbalanced state, leading to the expansion of the material due to high pressure. In this way, most of the absorbed laser energy can be removed from the material by the ejection of matter, and thus the heat-affected zone in femtosecond micromachining generally is so narrow that only minor damage to the material can occur (Fig. 10).

4. Conclusion

Within this work, we have studied the possibility of localised sculpture of the electrochemical activity of 3D-printed CB-PLA electrodes, and have differentiated the ablation effects by femtosecond (FSL) and nanosecond laser.

Our measurements made it possible to optimise the operating conditions by the FSL and conclude that the electrochemical behaviour largely depends on the laser pulsed energy used. The CV and EIS data analysis revealed that modifying this parameter significantly influences the electrochemically active surface area (EASA) and to a less extent the

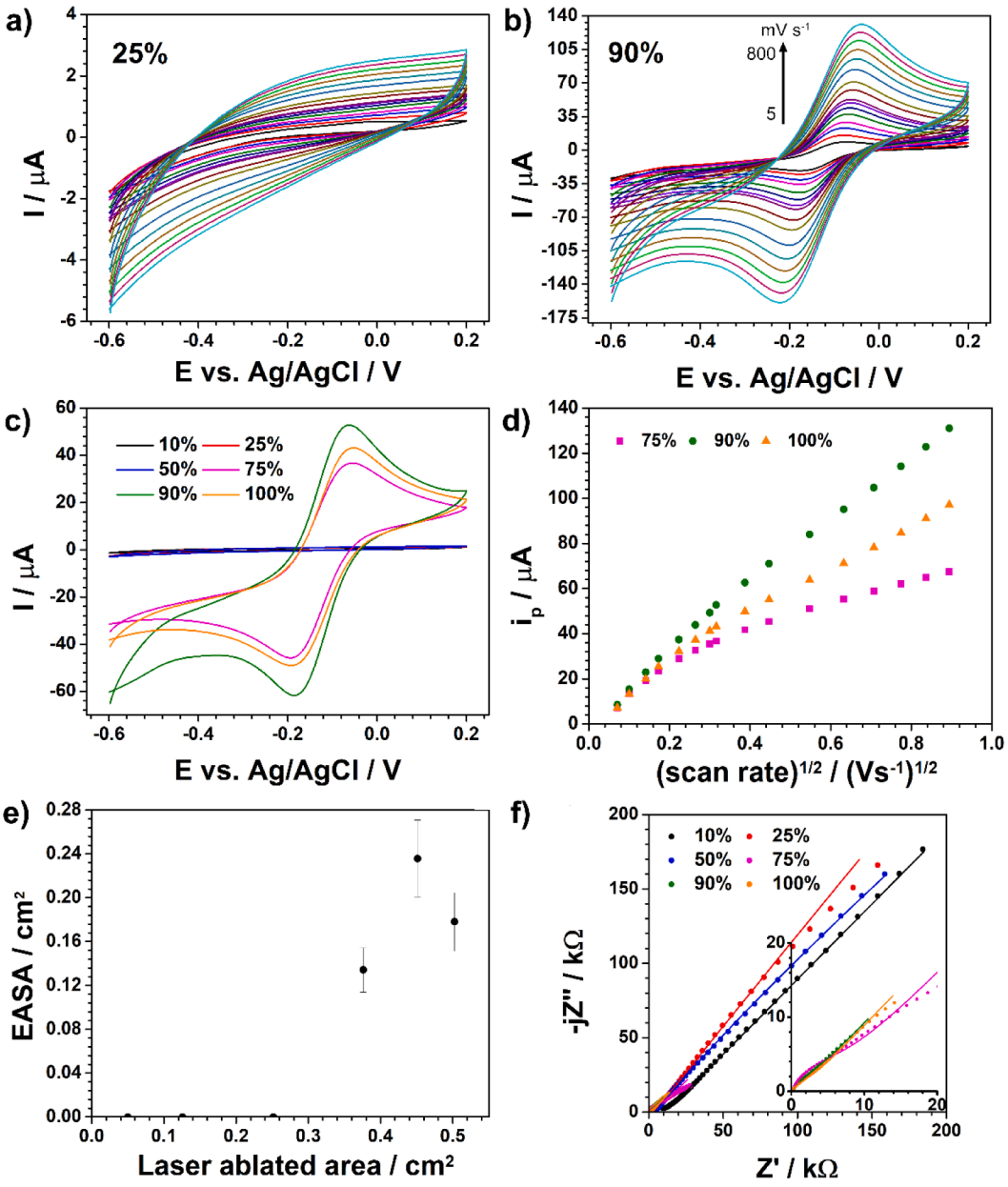

Fig. 8. (a,b) – CVs at different scan rates for CB-PLA electrodes with Nd:YAG-ablated shares of 25% and 100% of the electrolyte-exposed surface, respectively, and (c) CVs comparison (at 100 mV s^{-1}) for different shares of Nd:YAG-ablated areas, (d) peak current i_p vs scan rate square root $\upsilon^{1/2}$ relationship, (e) resultant relationship between EASA and FSL-ablated electrode area, (f) EIS spectra for CB-PLA with different shares of Nd:YAG-ablated surface areas. In EIS spectra points mark experimental results, solid line the EEC fitting. Electrolyte 1 mM $[Ru(NH_3)_6]^{2+/3+}$ in 0.1 M KCl. Nd:YAG operating parameters: number of pulses = 20, E_i = 0.64 J cm^{-2}.

charge transfer kinetics. In the case of the optimised FSL ablation conditions – 4.1 J cm^{-2} – the R_{CT} parameter dropped down to 7.8 kΩ, over one order of magnitude compared to the untreated electrode, with the CV peak separation ΔE = 96 mV for the hexaammineruthenium redox probe system. In this case, the estimated heterogeneous rate constant reaches $7.98 \bullet 10^{-3}$ cm s^{-1}. Importantly, CVs revealed hindered charge transfer mechanism and lower rate constants after Nd:YAG ablation ($k^0 = 2.66 \bullet 10^{-3}$ cm s^{-1}). This effect is followed by the rise of electric double layer quasi-capacitance Q. The PLA evaporation by FSL ablation reveals conductive CB nanoparticles, with only negligible changes due to oxidation by the FSL, as confirmed by SEM and XPS examination, respectively.

Next, localised sculpture of only a fraction of the electrolyte-exposed surface area reveals high linearity with an efficient EASA value, as calculated from the CVs. The EASA was approximately 40% of the geometric surface area, lower than in the case of surface activation by electrolysis in an alkaline media, based on other literature reports. The linearity of the above-mentioned function was only limited in the boundary conditions, when the activated area diameter was not greater than 2.5 mm. Notably, these conditions were only achieved in the case of the OSET probe, while the ISET probe revealed significantly higher randomisation of the results. We have also confirmed the local CB-PLA

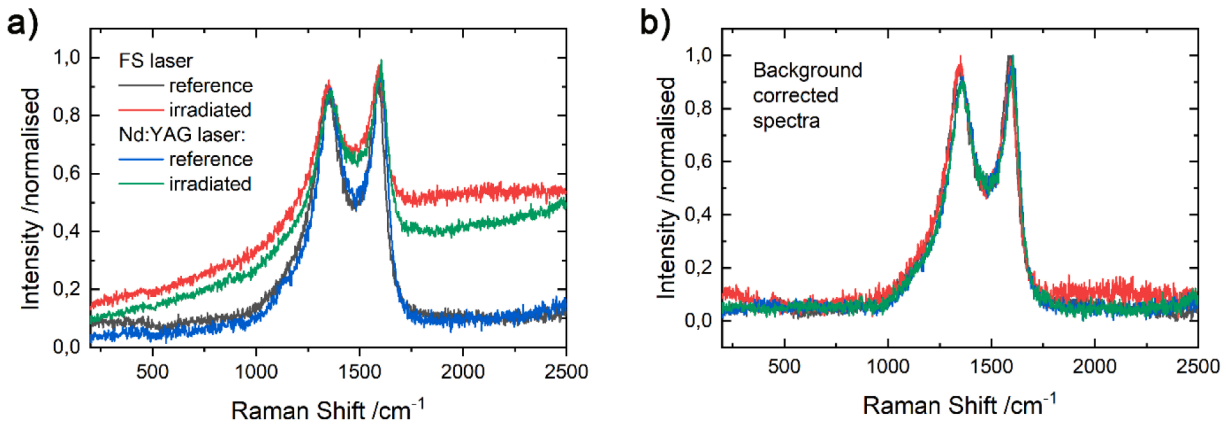

Fig. 9. (a) Raman spectra of a CB-PLA electrode surface before and after laser processing with FSL and Nd:YAG, (b) background corrected spectra.

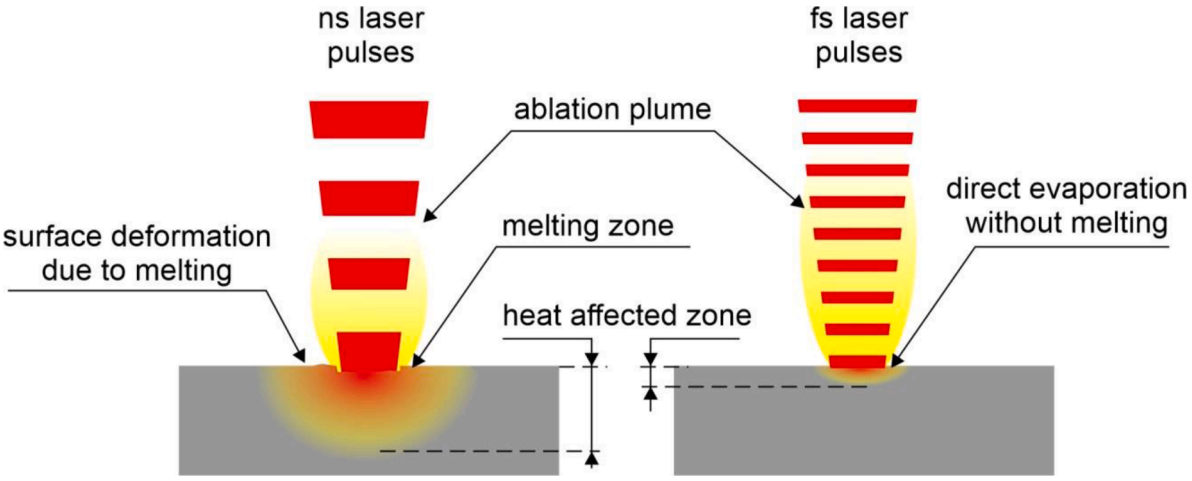

Fig. 10. Scheme visualising the differences between femto- and nanosecond laser beam interactions with matter.

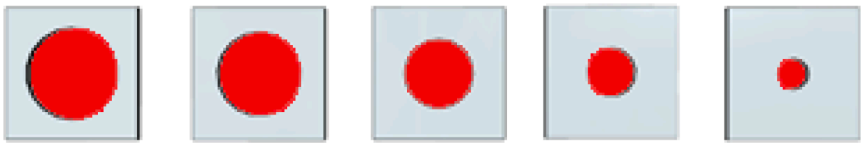

Scheme 1. Masks applied to CB-PLA electrodes to partially cover the surface area prior to activation.

sculpturing with the SECM images, after activating the surface area with a width as small as 0.2 mm, achieving the fastest kinetics with the effective rate constant k_{eff} of the FSL-ablated area reaching $3.6{\cdot}10^{-3}$ cm s^{-1}, as measured for ferrocenemethanol. On the other hand, the heterogeneous rate constant estimated for the hexaammineruthenium system from CVs reach up to $5.3{\cdot}10^{-3}$ cm s^{-1}, but is smaller and equal to 1.06 cm s^{-1} for small FSL-ablated electrode areas.

The significant differences in the heat-affected zone provide the most plausible conclusion about the different effects of the FSL and Nd:YAG laser ablation at the CB-PLA electrode surface. Unlike the FSL, when most of the absorbed laser energy contributed to the PLA evaporation, the heat transferred to the electrode surface during Nd:YAG treatment contributed to partial melting and re-solidification of the PLA. These thermal processes lead to CB-PLA surface oxidation and introduced a random factor to the resultant electrochemical activity of the electrode. The effect was particularly visible in the case of the localised surface ablation process by the Nd:YAG laser, as the polymer that melted within the heat-affected zone re-covered the conductive CB nanoparticles, hindering the electrode kinetics.

CRediT authorship contribution statement

Mateusz Cieslik: Methodology, Validation, Formal analysis, Investigation, Resources, Writing – original draft, Visualization. **Miroslaw Sawczak:** Methodology, Investigation, Writing – original draft, Writing – review & editing. **Rafal Jendrzejewski:** Investigation, Writing – original draft, Writing – review & editing. **Joanna Celej:** Investigation, Validation. **Wojciech Nogala:** Software, Writing – original draft, Writing – review & editing, Visualization. **Jacek Ryl:** Conceptualization, Investigation, Data curation, Writing – original draft, Writing – review & editing, Supervision, Project administration, Funding acquisition.

Declaration of Competing Interest

The authors declare that they have no known competing financial interests or personal relationships that could have appeared to influence the work reported in this paper.

Acknowledgements

Authors are grateful to Dr Monika Janik for her assistance in sample preparation. This work was supported by The National Science Centre (Republic of Poland) under project SONATA BIS number 2020/38/E/ST8/00409. The support of the Rector of the Gdańsk University of Technology to equip the scanning electrochemical microscopy laboratory within the GUT is greatly acknowledged. We are grateful to NKT Photonics A/S and Eurotek International Sp. z o.o. for the ORIGAMI XP femtosecond laser rental.

Supplementary materials

Supplementary material associated with this article can be found, in the online version, at doi:10.1016/j.electacta.2022.140288.

References

[1] V. Gjokaj, C. Crump, B. Wright, P. Chahal, Direct printing of antennas on large 3D printed plastic structures, in: Proceedings of the IEEE 70th Electronic Components and Technology Conference (ECTC), Orlando, FL, USA, IEEE, 2020, pp. 666–670, https://doi.org/10.1109/ECTC32862.2020.00110.

[2] S.C. Joshi, A.A. Sheikh, 3D printing in aerospace and its long-term sustainability, Virtual Phys. Prototyp. 10 (2015) 175–185, https://doi.org/10.1080/17452759.2015.1111519.

[3] E. Sacco, S.K. Moon, Additive manufacturing for space: status and promises, Int. J. Adv. Manuf. Technol. 105 (2019) 4123–4146, https://doi.org/10.1007/s00170-019-03786-z.

[4] J.S. Walker, J. Arnold, C. Shrestha, D. Smith, Antibacterial silver submicron wire-polylactic acid composites for fused filament fabrication, RPJ 26 (2020) 32–38, https://doi.org/10.1108/RPJ-04-2019-0100.

[5] C. Wang, W. Huang, Y. Zhou, L. He, Z. He, Z. Chen, X. He, S. Tian, J. Liao, B. Lu, Y. Wei, M. Wang, 3D printing of bone tissue engineering scaffolds, Bioact. Mater. 5 (2020) 82–91, https://doi.org/10.1016/j.bioactmat.2020.01.004.

[6] Q. Gu, J. Hao, Y. Lu, L. Wang, G.G. Wallace, Q. Zhou, Three-dimensional bio-printing, Sci. China Life Sci. 58 (2015) 411–419, https://doi.org/10.1007/s11427-015-4850-3.

[7] N. Lazarus, S.S. Bedair, Creating 3D printed sensor systems with conductive composites, Smart Mater. Struct. 30 (2021), 015020, https://doi.org/10.1088/1361-665X/abcbe2.

[8] S.W. Kwok, K.H.H. Goh, Z.D. Tan, S.T.M. Tan, W.W. Tjiu, J.Y. Soh, Z.J.G. Ng, Y. Z. Chan, H.K. Hui, K.E.J. Goh, Electrically conductive filament for 3D-printed circuits and sensors, Appl. Mater. Today 9 (2017) 167–175, https://doi.org/10.1016/j.apmt.2017.07.001.

[9] P.F. Flowers, C. Reyes, S. Ye, M.J. Kim, B.J. Wiley, 3D printing electronic components and circuits with conductive thermoplastic filament, Addit. Manuf. 18 (2017) 156–163, https://doi.org/10.1016/j.addma.2017.10.002.

[10] A. Abdalla, H.H. Hamzah, O. Keattch, D. Covill, B.A. Patel, Augmentation of conductive pathways in carbon black/PLA 3D-printed electrodes achieved through varying printing parameters, Electrochim. Acta 354 (2020), 136618, https://doi.org/10.1016/j.electacta.2020.136618.

[11] M.A.B. Helú, L. Liu, Fused deposition modeling (FDM) based 3D printing of microelectrodes and multi-electrode probes, Electrochim. Acta 365 (2021), 137279, https://doi.org/10.1016/j.electacta.2020.137279.

[12] S. Wickramasinghe, T. Do, P. Tran, FDM-based 3D printing of polymer and associated composite: a review on mechanical properties, defects and treatments, Polymers 12 (2020) 1529, https://doi.org/10.3390/polym12071529 (Basel).

[13] C.W. Foster, M.P. Down, Y. Zhang, X. Ji, S.J. Rowley-Neale, G.C. Smith, P.J. Kelly, C.E. Banks, 3D printed graphene based energy storage devices, Sci. Rep. 7 (2017) 42233, https://doi.org/10.1038/srep42233.

[14] F. Zhang, M. Wei, V.V. Viswanathan, B. Swart, Y. Shao, G. Wu, C. Zhou, 3D printing technologies for electrochemical energy storage, Nano Energy 40 (2017) 418–431, https://doi.org/10.1016/j.nanoen.2017.08.037.

[15] P. Chang, H. Mei, S. Zhou, K.G. Dassios, L. Cheng, 3D printed electrochemical energy storage devices, J. Mater. Chem. A 7 (2019) 4230–4258, https://doi.org/10.1039/C8TA11860D.

[16] L.F. Chen, Y. Feng, H.W. Liang, Z.Y. Wu, S.H. Yu, Macroscopic-scale three-dimensional carbon nanofiber architectures for electrochemical energy storage devices, Adv. Energy Mater. 7 (2017), 1700826, https://doi.org/10.1002/aenm.201700826.

[17] C.L. Manzanares Palenzuela, F. Novotný, P. Krupička, Z. Sofer, M. Pumera, 3D-printed graphene/polylactic acid electrodes promise high sensitivity in electroanalysis, Anal. Chem. 90 (2018) 5753–5757, https://doi.org/10.1021/acs.analchem.8b00083.

[18] C.W. Foster, H.M. Elbardisy, M.P. Down, E.M. Keefe, G.C. Smith, C.E. Banks, Additively manufactured graphitic electrochemical sensing platforms, Chem. Eng. J. 381 (2020), 122343, https://doi.org/10.1016/j.cej.2019.122343.

[19] D.P. Rocha, A.L. Squissato, S.M. da Silva, E.M. Richter, R.A.A. Munoz, Improved electrochemical detection of metals in biological samples using 3D-printed electrode: chemical/electrochemical treatment exposes carbon-black conductive sites, Electrochim. Acta 335 (2020), 135688, https://doi.org/10.1016/j.electacta.2020.135688.

[20] R.M. Cardoso, S.V.F. Castro, M.N.T. Silva, A.P. Lima, M.H.P. Santana, E. Nossol, R. A.B. Silva, E.M. Richter, T.R.L.C. Paixão, R.A.A. Muñoz, 3D-printed flexible device combining sampling and detection of explosives, Sens. Actuators B Chem. 292 (2019) 308–313, https://doi.org/10.1016/j.snb.2019.04.126.

[21] R.M. Cardoso, D.M.H. Mendonça, W.P. Silva, M.N.T. Silva, E. Nossol, R.A.B. da Silva, E.M. Richter, R.A.A. Muñoz, 3D printing for electroanalysis: from multiuse electrochemical cells to sensors, Anal. Chim. Acta 1033 (2018) 49–57, https://doi.org/10.1016/j.aca.2018.06.021.

[22] M.J. Glowacki, M. Cieslik, M. Sawczak, A. Koterwa, I. Kaczmarzyk, R. Jendrzejewski, L. Szynkiewicz, T. Ossowski, R. Bogdanowicz, P. Niedzialkowski, J. Ryl, Helium-assisted, solvent-free electro-activation of 3D printed conductive carbon-polylactide electrodes by pulsed laser ablation, Appl. Surf. Sci. 556 (2021), 149788, https://doi.org/10.1016/j.apsusc.2021.149788.

[23] G.D. O'Neil, S. Ahmed, K. Halloran, J.N. Janusz, A. Rodríguez, I.M. Terrero Rodríguez, Single-step fabrication of electrochemical flow cells utilizing multi-material 3D printing, Electrochem. Commun. 99 (2019) 56–60, https://doi.org/10.1016/j.elecom.2018.12.006.

[24] E. Vaněčková, M. Bouša, F. Vivaldi, M. Gál, J. Rathouský, V. Kolivoška, T. Sebechlebská, UV/VIS spectroelectrochemistry with 3D printed electrodes, J. Electroanal. Chem. 857 (2020), 113760, https://doi.org/10.1016/j.jelechem.2019.113760.

[25] E. Vaněčková, M. Bouša, Š. Nováková Lachmanová, J. Rathouský, M. Gál, T. Sebechlebská, V. Kolivoška, 3D printed polylactic acid/carbon black electrodes with nearly ideal electrochemical behaviour, J. Electroanal. Chem. 857 (2020), 113745, https://doi.org/10.1016/j.jelechem.2019.113745.

[26] A. Koterwa, I. Kaczmarzyk, S. Mania, M. Cieslik, R. Tylingo, T. Ossowski, R. Bogdanowicz, P. Niedziałkowski, J. Ryl, The role of electrolysis and enzymatic hydrolysis treatment in the enhancement of the electrochemical properties of 3D-printed carbon black/poly(lactic acid) structures, Appl. Surf. Sci. 574 (2022), 151587, https://doi.org/10.1016/j.apsusc.2021.151587.

[27] J. Luo, H. Wang, D. Zuo, A. Ji, Y. Liu, Research on the application of MWCNTs/PLA composite material in the manufacturing of conductive composite products in 3D printing, Micromachines 9 (2018) 635, https://doi.org/10.3390/mi9120635.

[28] M.P. Browne, F. Novotný, Z. Sofer, M. Pumera, 3D printed graphene electrodes' electrochemical activation, ACS Appl. Mater. Interfaces 10 (2018) 40294–40301, https://doi.org/10.1021/acsami.8b14701.

[29] S. Sato, D. Gondo, T. Wada, S. Kanehashi, K. Nagai, Effects of various liquid organic solvents on solvent-induced crystallization of amorphous poly(lactic acid) film, J. Appl. Polym. Sci. 129 (2013) 1607–1617, https://doi.org/10.1002/app.38833.

[30] Y. Wang, S. Su, L. Cai, B. Qiu, N. Wang, J. Xiong, C. Yang, X. Tao, Y. Chai, Monolithic Integration of all-in-one supercapacitor for 3D electronics, Adv. Energy Mater. 9 (2019), 1900037, https://doi.org/10.1002/aenm.201900037.

[31] C. Zhu, T. Liu, F. Qian, W. Chen, S. Chandrasekaran, B. Yao, Y. Song, E.B. Duoss, J. D. Kuntz, C.M. Spadaccini, M.A. Worsley, Y. Li, 3D printed functional nanomaterials for electrochemical energy storage, Nano Today 15 (2017) 107–120, https://doi.org/10.1016/j.nantod.2017.06.007.

[32] P.L. dos Santos, V. Katic, H.C. Loureiro, M.F. dos Santos, D.P. dos Santos, A.L. B. Formiga, J.A. Bonacin, Enhanced performance of 3D printed graphene electrodes after electrochemical pre-treatment: role of exposed graphene sheets, Sens. Actuators B Chem. 281 (2019) 837–848, https://doi.org/10.1016/j.snb.2018.11.013.

[33] C.L. Manzanares-Palenzuela, S. Hermanova, Z. Sofer, M. Pumera, Proteinase-sculptured 3D-printed graphene/polylactic acid electrodes as potential biosensing platforms: towards enzymatic modeling of 3D-printed structures, Nanoscale 11 (2019) 12124–12131, https://doi.org/10.1039/C9NR02754H.

[34] K. Sugioka, M. Meunier, A. Piqué (Eds.), Laser Precision Microfabrication, Springer Berlin Heidelberg, Berlin, Heidelberg, 2010, https://doi.org/10.1007/978-3-642-10523-4.

[35] B.N. Chichkov, C. Momma, S. Nolte, F. Alvensleben, A. Tünnermann, Femtosecond, picosecond and nanosecond laser ablation of solids, Appl. Phys. A 63 (1996) 109–115, https://doi.org/10.1007/BF01567637.

[36] Y. Liu, P. Liu, W. Qin, X. Wu, G. Yang, Laser modification-induced $NiCo_2O_4$-δ with high exterior Ni^{3+}/Ni^{2+} ratio and substantial oxygen vacancies for electrocatalysis, Electrochim. Acta 297 (2019) 623–632, https://doi.org/10.1016/j.electacta.2018.11.111.

[37] X. Wu, H. Yin, Q. Li, Ablation and patterning of carbon nanotube film by femtosecond laser irradiation, Appl. Sci. 9 (2019) 3045, https://doi.org/10.3390/app9153045.

[38] A. Abdelmalek, Z. Bedrane, E.H. Amara, B. Sotillo, V. Bharadwaj, R. Ramponi, S. Eaton, Ablation of copper metal films by femtosecond laser multipulse irradiation, Appl. Sci. 8 (2018) 1826, https://doi.org/10.3390/app8101826.

[39] C. Jing, Z. Wang, Y. Cheng, Characteristics and applications of spatiotemporally focused femtosecond laser pulses, Appl. Sci. 6 (2016) 428, https://doi.org/10.3390/app6120428.

[40] J. Cui, Y. Cheng, J. Zhang, H. Mei, X. Wang, Femtosecond laser irradiation of carbon nanotubes to metal electrodes, Appl. Sci. 9 (2019) 476, https://doi.org/10.3390/app9030476.

[41] D. Serien, H. Kawano, A. Miyawaki, K. Midorikawa, K. Sugioka, Femtosecond laser direct write integration of multi-protein patterns and 3D microstructures into 3D glass microfluidic devices, Appl. Sci. 8 (2018) 147, https://doi.org/10.3390/app8020147.

[42] J. Kanasaki, E. Inami, K. Tanimura, H. Ohnishi, K. Nasu, Formation of sp^3 -bonded carbon nanostructures by femtosecond laser excitation of graphite, Phys. Rev. Lett. 102 (2009), 087402, https://doi.org/10.1103/PhysRevLett.102.087402.

[43] V. Saikiran, M.H. Dar, D.N. Rao, Femtosecond laser induced nanostructuring of graphite for the fabrication of quasi-periodic nanogratings and novel carbon nanostructures, Appl. Surf. Sci. 428 (2018) 177–185, https://doi.org/10.1016/j.apsusc.2017.09.126.
[44] P. Moreno, C. Méndez, A. García, I. Arias, L. Roso, Femtosecond laser ablation of carbon reinforced polymers, Appl. Surf. Sci. 252 (2006) 4110–4119, https://doi.org/10.1016/j.apsusc.2005.06.008.
[45] C. NunesKirchner, K.H. Hallmeier, R. Szargan, T. Raschke, C. Radehaus, G. Wittstock, Evaluation of thin film titanium nitride electrodes for electroanalytical applications, Electroanalysis 19 (2007) 1023–1031, https://doi.org/10.1002/elan.200703832.
[46] W. Nogala, P. Kannan, S. Gawinkowski, M. Jönsson-Niedziolka, M. Kominiak, J. Waluk, M. Opallo, Tailored gold nanostructure arrays as catalysts for oxygen reduction in alkaline media and a single molecule SERS platform, Nanoscale 7 (2015) 10767–10774, https://doi.org/10.1039/C5NR02077H.
[47] R.S. Nicholson, Theory and application of cyclic voltammetry for measurement of electrode reaction kinetics, Anal. Chem. 37 (1965) 1351–1355, https://doi.org/10.1021/ac60230a016.
[48] J. Ryl, L. Burczyk, A. Zielinski, M. Ficek, A. Franczak, R. Bogdanowicz, K. Darowicki, Heterogeneous oxidation of highly boron-doped diamond electrodes and its influence on the surface distribution of electrochemical activity, Electrochim. Acta 297 (2019) 1018–1027, https://doi.org/10.1016/j.electacta.2018.12.050.
[49] S. Amand, M. Musiani, M.E. Orazem, N. Pébère, B. Tribollet, V. Vivier, Constant-phase-element behavior caused by inhomogeneous water uptake in anti-corrosion coatings, Electrochim. Acta 87 (2013) 693–700, https://doi.org/10.1016/j.electacta.2012.09.061.
[50] J. Ryl, J. Wysocka, M. Cieslik, H. Gerengi, T. Ossowski, S. Krakowiak, P. Niedzialkowski, Understanding the origin of high corrosion inhibition efficiency of bee products towards aluminium alloys in alkaline environments, Electrochim. Acta 304 (2019) 263–274, https://doi.org/10.1016/j.electacta.2019.03.012.
[51] D.J. Miller, M.C. Biesinger, N.S. McIntyre, Interactions of CO_2 and CO at fractional atmosphere pressures with iron and iron oxide surfaces: one possible mechanism for surface contamination? Surf. Interface Anal. 33 (2002) 299–305, https://doi.org/10.1002/sia.1188.
[52] M.P. Browne, V. Urbanova, J. Plutnar, F. Novotný, M. Pumera, Inherent impurities in 3D-printed electrodes are responsible for catalysis towards water splitting, J. Mater. Chem. A 8 (2020) 1120–1126, https://doi.org/10.1039/C9TA11949C.
[53] J. Wysocka, M. Cieslik, S. Krakowiak, J. Ryl, Carboxylic acids as efficient corrosion inhibitors of aluminium alloys in alkaline media, Electrochim. Acta 289 (2018) 175–192, https://doi.org/10.1016/j.electacta.2018.08.070.
[54] J.F.S. Pereira, R.G. Rocha, S.V.F. Castro, A.F. João, P.H.S. Borges, D.P. Rocha, A. de Siervo, E.M. Richter, E. Nossol, R.V. Gelamo, R.A.A. Muñoz, Reactive oxygen plasma treatment of 3D-printed carbon electrodes towards high-performance electrochemical sensors, Sens. Actuators B Chem. 347 (2021), 130651, https://doi.org/10.1016/j.snb.2021.130651.
[55] Y. Meng, M. Du, F. Cao, Influence of chloride ion adsorption on the kinetics and mechanism of Ru(NH3)63+/2+ electrode reactions, Electrochim. Acta 324 (2019), 134863, https://doi.org/10.1016/j.electacta.2019.134863.
[56] L. Huang, Y. Cao, D. Diao, Nanosized graphene sheets induced high electrochemical activity in pure carbon film, Electrochim. Acta 262 (2018) 173–181, https://doi.org/10.1016/j.electacta.2018.01.027.
[57] A.J. Bard, L.R. Faulkner, Electrochemical Methods: Fundamentals and Applications, 2nd ed., Wiley, New York, 2001.
[58] J. Ryl, A. Zielinski, L. Burczyk, R. Bogdanowicz, T. Ossowski, K. Darowicki, Chemical-assisted mechanical lapping of thin boron-doped diamond films: a fast route toward high electrochemical performance for sensing devices, Electrochim. Acta 242 (2017) 268–279, https://doi.org/10.1016/j.electacta.2017.05.027.
[59] R. Cornut, C. Lefrou, New analytical approximation of feedback approach curves with a microdisk SECM tip and irreversible kinetic reaction at the substrate, J. Electroanal. Chem. 621 (2008) 178–184, https://doi.org/10.1016/j.jelechem.2007.09.021.
[60] L.I. Stephens, N.A. Payne, S.A. Skaanvik, D. Polcari, M. Geissler, J. Mauzeroll, Evaluating the use of edge detection in extracting feature size from scanning electrochemical microscopy images, Anal. Chem. 91 (2019) 3944–3950, https://doi.org/10.1021/acs.analchem.8b05011.
[61] Y. Kameya, K. Hanamura, Kinetic and Raman spectroscopic study on catalytic characteristics of carbon blacks in methane decomposition, Chem. Eng. J. 173 (2011) 627–635, https://doi.org/10.1016/j.cej.2011.08.017.
[62] A.C. Ferrari, J.C. Meyer, V. Scardaci, C. Casiraghi, M. Lazzeri, F. Mauri, S. Piscanec, D. Jiang, K.S. Novoselov, S. Roth, A.K. Geim, Raman spectrum of graphene and graphene layers, Phys. Rev. Lett. 97 (2006), 187401, https://doi.org/10.1103/PhysRevLett.97.187401.
[63] W. Jia, Y. Luo, J. Yu, B. Liu, M. Hu, L. Chai, C. Wang, Effects of high-repetition-rate femtosecond laser micromachining on the physical and chemical properties of polylactide (PLA), Opt. Express 23 (2015) 26932, https://doi.org/10.1364/OE.23.026932.
[64] J. Morikawa, A. Orie, T. Hashimoto, S. Juodkazis, Thermal diffusivity in femtosecond-laser-structured micro-volumes of polymers, Appl. Phys. A 98 (2010) 551–556, https://doi.org/10.1007/s00339-009-5493-7.
[65] W. Rozmus, V.T. Tikhonchuk, R. Cauble, A model of ultrashort laser pulse absorption in solid targets, Phys. Plasmas 3 (1996) 360–367, https://doi.org/10.1063/1.871861.